Journal Pre-proof

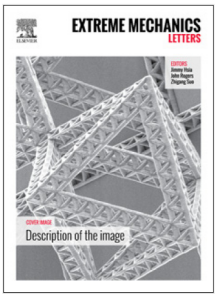

From rigid to amorphous folding behavior in origami-inspired metamaterials with bistable hinges

Agustin Iniguez-Rabago, Johannes T.B. Overvelde

PII: S2352-4316(22)00162-6
DOI: https://doi.org/10.1016/j.eml.2022.101881
Reference: EML 101881

To appear in: *Extreme Mechanics Letters*

Received date : 7 March 2022
Revised date : 21 July 2022
Accepted date : 9 August 2022

Please cite this article as: A. Iniguez-Rabago and J.T.B. Overvelde, From rigid to amorphous folding behavior in origami-inspired metamaterials with bistable hinges, *Extreme Mechanics Letters* (2022), doi: https://doi.org/10.1016/j.eml.2022.101881.

From rigid to amorphous folding behavior in origami-inspired metamaterials with bistable hinges

Agustin Iniguez-Rabago[1] and Johannes T.B. Overvelde[1,2]

[1] *Autonomous Matter Department, AMOLF, Science Park 104, 1098 XG Amsterdam, The Netherlands*
[2] *Institute for Complex Molecular Systems and Department of Mechanical Engineering, Eindhoven University of Technology, P.O. Box 513, 5600 MB Eindhoven, the Netherlands**

(Dated: July 21, 2022)

The folding behavior of origami-inspired metamaterials is often described by linear rotational springs and rigid faces. However, other folding modes and multistatbility appears when assuming elastic faces, specially when assuming (non-euclidean) crease patterns in 2D or 3D where a high number of hinges meet at their vertices. Instead, here we study multistability by exploring the use of non-linear material behavior implemented as bistable hinges. By drawing a similitude to atomic crystals, we are able to classify the complex folding behavior that non-linear elastic origami metamaterials undergo, where we identify transitions from rigid to elastic to amorphous behavior upon increasing the strength of the bistability. As a result, our study gives a better understanding and provides a tool to control multistable metamaterials for future applications.

The ancient art of origami is often used as inspiration for mechanisms that allow a sheet to transform into complex 3D shapes [1]. These mechanisms are interesting for the design of morphing structures with a wide range of applications [2, 3] spanning from heart stents [4] and intraocular implants [5] to airbags [6] and solar panel arrays for satellites [7]. The underlying foldable origami patterns are typically described by a set of rigid faces connected by linear or zero-stiffness rotational springs (i.e. rigid origami), and their folding behavior originates from the arrangement of the hinges. In this description, deformations are only allowed by folding a group of hinges through a limited number of pathways (i.e branches). Following such approach, origami structures can be designed to become flat foldable [8, 9], self-folding [10–12], pluripotent [13] or reconfigurable [14]. Nonetheless, if the hinges are not assigned with a mountain-valley configuration, folding an origami pattern from a flat state to a specific 3D shape is not straightforward as multiple branches meet at this state [15, 16].

When no longer assuming perfect rigidity of the faces (i.e. faces can stretch or bend) additional degrees of freedom appear that could guide the folding behavior of the flat structures. Such description, referred to as elastic origami, creates soft modes along the branches [17], while also supporting deformations outside of the soft modes. Moreover, reducing the constraints on the deformations opens up more folding pathways, allowing the sheets to reach multiple energy minima (i.e. multistability) that were hidden in the fully rigid origami description [18, 19]. Interestingly, these complex energy landscapes originate from geometrical features and have been studied for various origami structures based on prismatic building blocks [17], the square twist pattern [18], the Miura-ori pattern [20], and the hypar [21], among others [19, 22, 23].

* overvelde@amolf.nl

Here we introduce multistability in elastic origami by assuming bistable hinge behavior. The goal of this study is to describe and understand the interactions between these non-linear hinges in elastic origami and their effect on the self-folding behavior of initially flat sheets. To extract and classify interesting behaviors that could result from such interactions, we focus our work on a relatively simple double-symmetric 4-vertex origami. This design has previously been described in the rigid origami regime [24, 25] and can be used as a first exploration to study how non-linearity can select certain stable pathways and states over others. However, the interaction between the non-linear and the elastic behavior is not restricted to this model and can potentially occur in any elastic metamaterial that exhibits pre-stress, e.g., through local actuation or external loading.

Our findings in this study are mostly obtained using a numerical model that predicts the deformation of the origami-inspired metamaterial, which we qualitatively validate by performing experiments. In particular, by varying the strength of the bistability, both numerically and experimentally, we probe the potential behavior of the origami-inspired sheets, where we employ analysis methods used for 2D atomic crystal lattices to identify several regimes in their behavior, and the corresponding limitations.

Bistable origami hinges.—Each origami tessellation can be represented by a set of hinges. To achieve non-linear behavior, each hinge is represented as a rotational spring characterized by a symmetric double-well potential energy E_h following

$$E_\mathrm{h} = k_\mathrm{h} \frac{(\theta^2 - \Theta^2)^2}{(\Theta)^4}, \tag{1}$$

in which θ is the fold angle. We define the energy to be zero at the rest angles Θ and $-\Theta$, with an energy barrier of k_h (Fig. 1a), making the hinge bistable. Note that the hinge is at the top of the energy barrier when placed in its flat state, and has equal probability of folding either way.

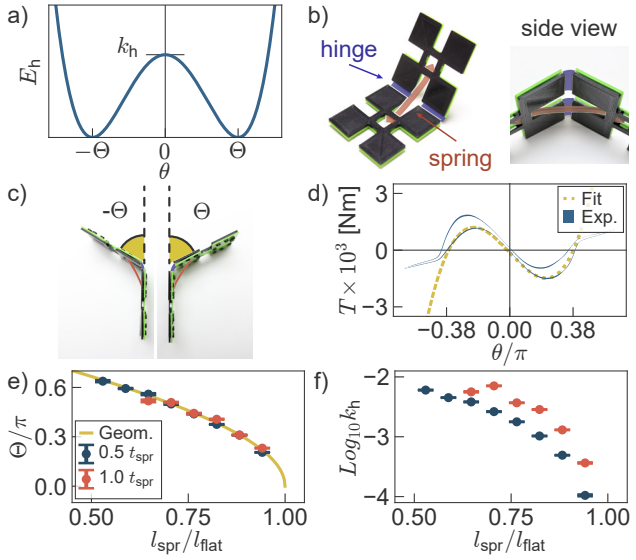

FIG. 1. a) Energy of the bistable hinge modeled as a symmetric double-well potential. b) Experimental realization of a bistable hinge made by connecting two rigid faces ($37 \times 37 \times 2.5$ mm PLA) with an elastic hinge (0.5 mm thick and 4 mm wide silicon elastomer) and a pre-stretched spring (t_{spr} thick and l_{spr} long silicon elastomer). c) The two stable states of the bistable hinge are characterized by a folding angle Θ. d) Relation between the measured average torque T and hinge angle θ obtained by cyclic loading (five times) of a hinge with $t_{spr} = 0.5$ mm and $l_{spr}/l_{flat} = 0.82$, fitted by our model. The standard deviation in experiments is indicated by the thickness of the line. Fit of e) the rest angle Θ and f) the energy barrier k_h for different l_{spr} and t_{spr}, where the errorbars are determined from the diagonals of the covariance matrix.

Experimentally, such a bistable hinge can be fabricated by connecting two rigid faces with an elastic hinge [17] and a pre-stretched spring (Fig. 1b and Supplemental Material: *Experiments*). Importantly, this hinge has two stable positions corresponding to the hinge folding to Θ and $-\Theta$ (Fig. 1c). We characterized a bistable hinge by measuring the relation between torque and fold angle using a rotational test machine (Supplemental Material: *Experiments*). Fig. 1d shows the average response of a hinge with $t_{spr} = 0.5$ mm and $l_{spr}/l_{flat} = 0.82$, where $l_{flat} = 34$ mm is the spring length when the fold angle $\theta = 0$. Note that we observe two distinct regions in the torque-angle response of the bistable hinge. First, for angles close to zero the hinge behaves as our double-well potential. Second, for larger angles the spring no longer contributes to the total energy since it is no longer stretched. The energy can therefore be described by only the linear behavior of the silicone elastomer hinge.

Furthermore, the bistable behavior of the hinge can be relatively easily changed by varying the rest length l_{spr} and thickness t_{spr} of the pre-stretched spring. We exemplified these results in Fig. 1e-f by performing additional experiments for a range of l_{spr}, and fitting the data to our double-well potential for small angles (Supplemental Material: *Experiments*).

Combining hinges into a single vertex.—To start exploring interactions between multiple hinges, we combine four of these non-linear hinges into a double-symmetric 4-vertex [24] (Fig. 2a). While typically in elastic origami faces can bend and stretch, here we only incorporate the stretchability of the faces [17]. This simplifies the model and reduces the degrees of freedom of the system. We achieve this by constraining the face bending, since such deformation could be modeled by using an additional hinge [26], which would change the design of our vertex. Moreover, we also do not take into account the dynamics during folding [27], as this would increase the computational requirement considerably, and we are mostly interested in the potential stable states that could be reached. Note that this model can no longer be considered as a thin sheet model that is often used in origami, however, the face stretching can be interpreted as twisting and stretching of the hinges in experiments [17, 28]. For the sake of simplicity, we will still refer our system as origami. The stretching of the faces is modeled by placing linear springs with stiffness k_s along the edges (Fig. 2a), introducing stretch energy E_s (Supplemental Material: *Simulations*). As a result, the vertex' elastic energy ($E = E_h + E_s$) depends on two stiffness parameters k_s and k_h, and the rest angle Θ. Importantly, the stiffness parameters can be reduced to a single parameter $\kappa = k_h/k_s$, which defines the strength of the bistable behavior, and can be used to vary the behavior of the vertex between rigid and elastic. Note that for the simulations $L = 1$, so the normalization of k_s with respect to L has the same value and therefore κ is dimensionless.

To determine the folding behavior of the 4-vertex and the probability to find it in a certain state, we use Monte Carlo simulations. Assuming an initial hinge length equal to L, we randomly perturb the nodal positions around the flat state using a normal distribution with a standard deviation of $0.2L$ (Supplemental Material: *Simulations*), which is approximately similar to an imperfect flattening of the vertex in experiments. Next, we release the hinges and let the vertex relax to its local energy minimum using a Sequential Quadratic Programming algorithm (Supplemental Material: *Simulations*). We repeat this method $N_{sim} = 1000$ times for a range of combinations of κ and Θ, and use a two-step clustering algorithm to identify the stable states (Supplemental Material: *Simulations*). We find that the vertex deforms into 16 different stable states when starting from a nearly flat state. However, by considering symmetries we can reduce them to four unique stable states (Fig. 2b), which we refer to as the *Fold* (F), the *Dome* (D), the *Saddle* (S) and the *Miura-ori* (M) state.

To demonstrate the existence of the stable states found in simulations, we fabricate two prototypes of the double-symmetric 4-vertex by combing four bistable hinges (Fig. 2d), where we use $l_{spr} = 30$ mm and $l_{spr} = 18$ mm to obtain $\Theta \approx 0.3\pi$ and $\Theta \approx 0.6\pi$, respectively. As a

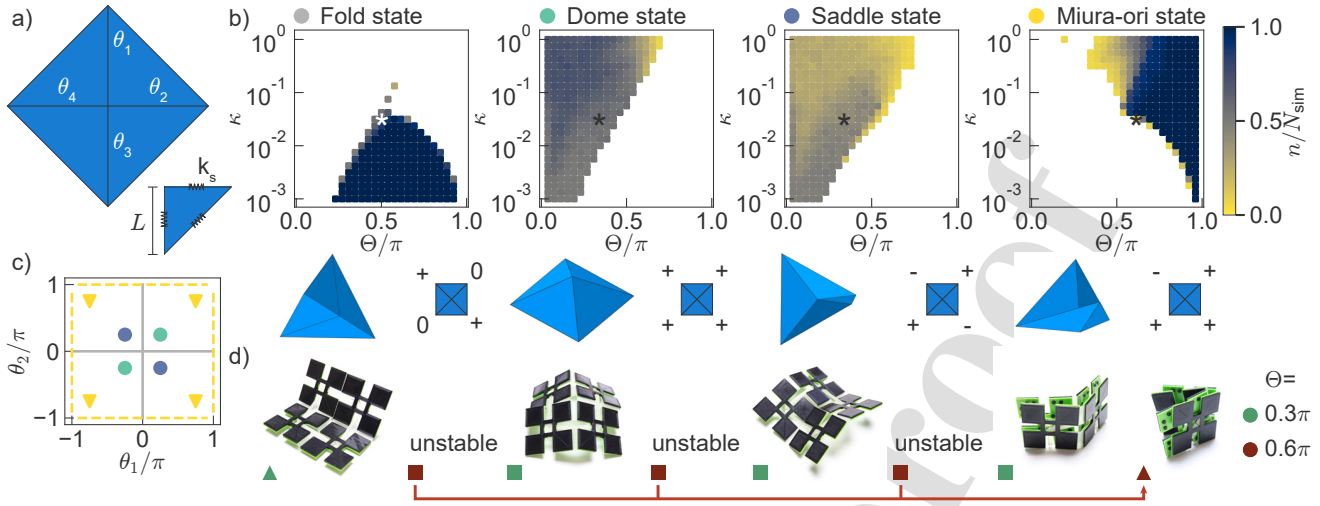

FIG. 2. a) Schematic of a double-symmetric 4-vertex with hinge angles θ_{1-4} and edges with linear spring stiffness k_s and initial length L. b) Relative appearance of the four different stable states against the two control parameters Θ and κ. Examples of the deformed stable states and the corresponding hinge orientation (0, + or -) are shown for the parameters indicated by the asterisk symbol. c) Branches (solid lines) and sub-branches (dashed lines) that exists for the 4-vertex, obtained by assuming a rigid origami description. When assuming an elastic origami description, the hinge angles tend to the circles ($\Theta = 0.25\pi$) or inverted triangles ($\Theta = 0.75\pi$). d) Experiments of two different prototypes of the vertices characterized by rest angles $\Theta \approx 0.3\pi$ and $\Theta \approx 0.6\pi$. Triangles show results from experiments in which the vertex was flattened and released, while squares show experiments in which the vertex was manually deformed towards the potential stable state prior to release.

first experiment, we flattened both vertices on a surface, and quickly released them (Movie 1), approximating the initial conditions used in the simulations. The results are presented in Fig. 2d and marked with a triangle. We observed that after the release from the flat configuration the vertex with $\Theta \approx 0.3\pi$ always folds to the Fold state, while the vertex with $\Theta \approx 0.6\pi$ folds into the Miura-ori state. Note that in this experiment the dynamic behavior of the vertex after the release dictates the folding path and the resulting stable state as it snaps to the final deformation. For this reason, we decided to perform a second experiment to further scan the existing stable states for each prototype. For this, we manually deformed the vertices into the remaining three states (marked with a square in Fig. 2d). We found that for $\Theta \approx 0.3\pi$ the vertex is stable in all configurations. In contrast, for $\Theta \approx 0.6\pi$ the vertex always snaps to the Miura-ori state, indicating that other states are unstable and the Miura-ori state is the only stable state for this particular design.

Based purely on the observed stable states and the measurements of the rest angle in Fig. 1d, we can qualitatively match our prototypes with a vertex for which $\kappa \approx 10^{-1.5}$ in our simulations. It is important to note that our simulations only capture partially the observed behavior in experiments, and therefore this value of κ only provides a rough comparison. Specifically, in experiments face bending will never be infinitely rigid, and face stretching effectively occurs mostly at the hinges as the hinges have a finite size [28]. In fact, these hinges still allow out-of-plane deformation and will buckle under compression, which are effects not captured in our model (Supplemental Material: *Experiments*). Such behavior could be captured by introducing additional springs to model the hinges [29].

Rigid and elastic vertex behavior.—We can divide the four stable states we found in simulations and experiments into two categories, depending on the origin of the stability. In the first category, the stable states originate from a rigid origami description. In this description, the double-symmetric 4-vertex has two main branches, and four sub-branches (Fig. 2c) [24]. Therefore, this category comprehends the Fold and the Miura-ori state corresponding to the main branches (solid) and the sub-branches (dashed), respectively (Fig. 2c). Note that we define the Miura-ori state as a state where one angle has opposite sign compared to the other angles, and does not necessary imply the typical Miura-ori design [7]. One characteristic of these states is that the elastic energy increases with an increase in κ (Supplemental Material: Fig. S8), since the faces do not deform and as such the stretch energy $E_s \approx 0$.

The second category comprises states that require face stretching. These states are the result of the elastic origami description combined with the torque resulting from the bistability. The elasticity transforms the branches and sub-branches of the vertex into soft modes, such that deformation outside of the branches is allowed. Since the bistability forces all the fold angles θ_{1-4} towards $\pm\Theta$ ($E_h \approx 0$), face stretching occurs. For example, when $\Theta = 0.25\pi$ (or 0.75π) the fold angles of the vertex try to move to the circular (or inverted triangular) markers in Fig. 2c, which lie outside of the branches

originating from a rigid origami description. The stable states corresponding to this category are the Dome, the Saddle and the Miura-ori states. They correspond to all possible sign combinations of the rest angles that do not require face crossing [30]. The energy of these states is characterized by a dependency on Θ (and not on κ) since their elastic energy is dominated by the stretch energy $E \approx E_s$ (Supplemental Material: Fig. S8). Note that the Miura-ori state belongs to both categories since it is related to both the rigid origami sub-branches, while also exhibiting considerable face deformations for a range of parameters, making it dependent on both Θ and κ.

Analysis of vertex tessellations.—Having characterized the stable states and their origin for a 4-vertex, the next step is to tessellate this vertex in a square lattice, effectively creating a mechanical metamaterial [31]. By doing so, we can determine how the vertices interact with each other in such a material and how this affects the overall folding behavior. We first focus on a square lattice that consists of 4×4 vertices (Fig. 3a), where we set $\Theta = 0.25\pi$ and $\kappa = 10^{-1.5}$ according to approximated values based on the experiments of a single vertex. Starting from the flat configuration, we perform the same Monte Carlo simulation as for the single vertex.

To characterize the stable states of the material and to determine whether the folding behavior originates from a rigid or elastic framework, we first analyze the state of each vertex in the deformed material. We use the second step of the clustering algorithm previously employed (Supplemental Material: *Simulations*), from which we get a 4×4 state matrix. Each entry of this matrix represents one of the four potential stable states of the vertex (Fig. 2b). Moreover, for each entry we also consider the orientation of the stable state. Here, the Fold state has two directions ($|$ and $-$), the Dome and Saddle state are symmetric in all directions, and the Miura-ori state has four directions ($>$, $<$, $\wedge$ and $\vee$) as illustrated in Fig. 3b. Note that all states have a positive and negative orientation, depending to which side the hinge folds (either $+$ or $-$), but to simplify the analysis we consider both to be symmetric. Interestingly, we find that the stable states of the material follow two different behaviors. Most of the simulations result in a stable state whose state matrix has a periodicity smaller than the total size of the metamaterial, while the other simulations present folding patterns with similar periodicities separated by boundaries (Fig. 3c).

To analyze and understand these results, we draw a similitude of our multistable origami metamaterials to 2D atomic crystal lattices. We let each vertex of our metamaterial correspond to an atom position and each stable vertex state to a different type of atom (Fig. 3b). The combination of these stable states in the specific vertex position can form periodic origami crystals with defined unit cells, just as a combination of atoms can form periodic crystals. Furthermore, as with atoms [32], these origami crystals can have defects. Specifically, only two kinds of defects can occur: crystal boundaries between the same type of crystals, and boundaries between dissimilar crystals. Other possible atomic defects involve the addition or subtraction of atoms, which for our metamaterials implies the addition or subtraction of vertices and thus the change of the tessellation. Following the terminology used in 2D atomic crystal lattices, if the metamaterial has only one type of crystal with all unit cells oriented in the same direction we call it monocrystalline (mc), whereas if there is any type of defect we call the material polycrystalline (pc) (Fig. 3c).

Potential stable states in the tessellations.—When applying this classification to our simulated metamaterial, we obtain one type of crystal with a unit cell of 2×2 vertices (Fig. 3c), characterized by a checkerboard pattern of Dome and Saddle states that we call the *Dome-Saddle* (DS) crystal. In $n/N_{\text{sim}} = 0.81$ of the simulations (with $N_{\text{sim}} = 1000$ the number of performed simulations), we obtain a monocrystalline DS (mcDS) material, while in the remaining simulations we obtain polycrystalline materials with only one type of boundary. This boundary is characterized by two neighboring crystals that appear as mirrored images, thus we call it a twin boundary (DSt).

We then perform more simulations using a range of parameters in the search for other types of crystals. We select two rest angles $\Theta = 0.25\pi$ and $\Theta = 0.75\pi$ that correspond approximately to the rest angles of the experiments, while we vary κ. From these simulations, we identify two additional types of crystals, which we refer to as the *All-Fold* (AF), and the *All-Miura-ori* (AM) (Fig. 3d). These crystals have unit cell size equal to 1×1 and 2×2 (due to the $+/-$ symmetry), respectively. Note that for the AM crystal we observe two types of crystal boundaries: rotational (AMr) with rotated crystals at the boundary and mirror boundaries. We further identify two different mirror boundaries that result in a different folded shape, the twin (AMt) with longitudinal mirrored crystals, and slip (AMs) with shifted crystals (Fig. 3e and Supplemental Material: Fig. S9). These correspond to the three different arrangements that neighboring unit cells can have. Interestingly, the AF crystal does not show any defects in our simulations, which we correlate to the fact that the fold state comes from the rigid origami description. Furthermore, we find interfaces between AM and DS crystal (MDinter), and AM and AF crystals (MFinter), but not between DS and AF crystals (Fig. 3e and Supplemental Material: Fig. S9). These interfaces seem to only occur between crystals originating from the same description, MDinter from the elastic origami, and MFinter from the rigid origami description.

From these results we observe that at $\kappa = 10^{-1.5}$ the material forms only DS crystals at low Θ and both AM monocrystalline and polycrystalline patterns at high Θ. To demonstrate the existence of these crystals and crystal defects, we built a 4×4 material with vertices having low $\Theta \approx 0.3\pi$ and high $\Theta \approx 0.6\pi$. We first flattened the material and quickly released it (Movie 1), similar to the experiments performed for the single vertex. We find that the metamaterial with low Θ always folds to an

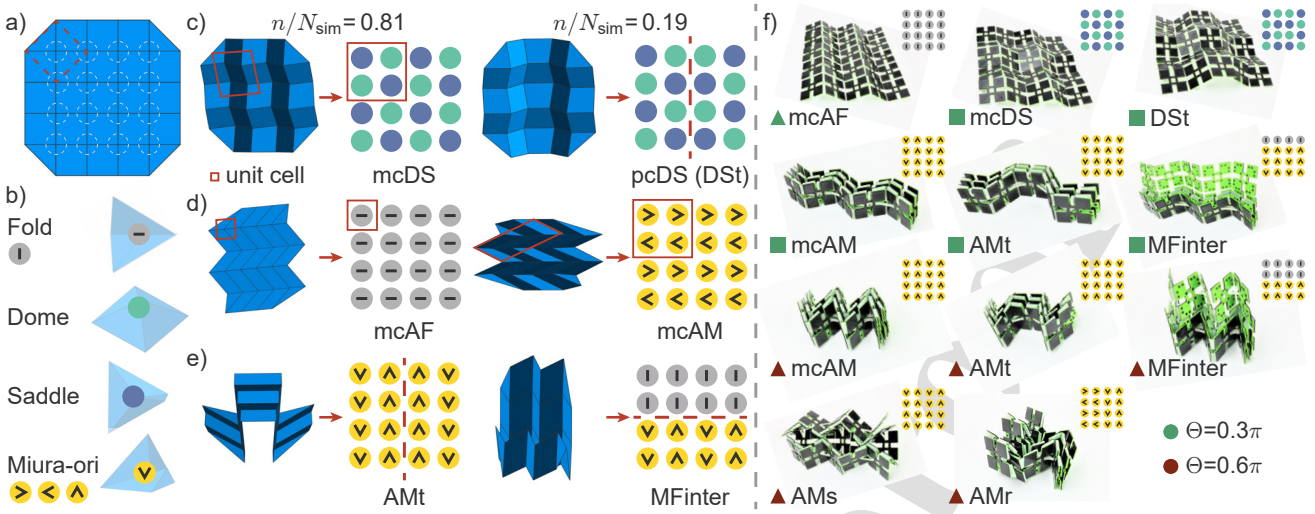

FIG. 3. a) Tessellation of a vertex (dashed red square) in a 4×4 lattice. Circles represent atom positions. b) Possible stable states (atom types) and orientations of a single vertex. c) Results of $N_{\text{sim}} = 1000$ simulations of a metamaterial with $\kappa = 10^{-1.5}$ and $\Theta = 0.25\pi$. d) Other observed monocrystalline materials found by varying κ for two rest angles $\Theta = 0.25\pi$ and $\Theta = 0.75\pi$. e) Example of a twin boundary (AMt) and an interface between different crystal types (MFinter) observed in pcAM crystals. f) Experimental validation of two metamaterials characterized by rest angles $\Theta = 0.3\pi$ and $\Theta = 0.6\pi$. Triangles show results from experiments in which the material was flattened and released, while squares show experiments in which the material was manually deformed towards the stable state prior to release.

mcAF material after the release from the flat configuration, while the metamaterial with high Θ folds to either a mcAM or a pcAM with all possible defects (AMr, AMt, AMs, and MFinter) as marked with a triangle in Fig. 3f. We next performed the second experiment where we deformed the material to specific states to obtain all possible stable states. For the low Θ metamaterial, we additionally obtained DS and AM crystals, both monocrystalline and polycrystalline with some defects (DSt, and AMt and MFinter, respectively) as marked with a square in Fig. 3f. On the contrary, for the high Θ material we did not obtain any additional crystal or crystal defects.

Similar to the single vertex experiment, the simulations for the metamaterials are a simplification of reality and therefore do not necessarily demonstrate the exact folding behavior observed in experiments. However, all material crystals and crystal defects are reached at both low and high Θ. These results match qualitatively with our simulations, and even though we cannot make quantitative predictions for which a more detailed model should be used [29], we find enough resemblance between the stable states observed in experiments and simulations. Therefore, we are confident that we get essential insights from the results obtained from simulations for which we can perform a larger number of studies, and explore a larger range of parameters or unit cells.

Rigid to elastic transition.—Next, to determine how the strength of the bistable hinges affects the behavior of the metamaterial, we identify all crystals and their defects of the previous parameter study (Supplemental Material: *Crystal characterization*). In Fig. 4a we show the percentage of simulations of the material with $\Theta = 0.25\pi$ (n/N_{sim}) that are either monocrystalline or polycrystalline, indicated for each crystal type. For low values of κ we only observe mcAF crystals. However, when increasing κ, a sudden transition occurs to a different crystalline metamaterial. We find that the mcAF state transitions to a mcDS state at $\kappa \approx 10^{-2.5}$. Interestingly, the transition happens at the same κ as in Fig. 2a when the single vertex goes from the Fold state to the Dome or Saddle state (for $\Theta = 0.25\pi$). We observe the same type of transition for a material with $\Theta = 0.75\pi$ (Fig. 4b). Both transitions are a clear indication of a transition from the rigid origami behavior represented by the mcAF crystal to an elastic origami behavior represented by either the DS crystal or AM crystal.

Elastic to amorphous transition.—Additionally, when increasing κ further, we notice that polycrystalline metamaterials start to appear, and the amount of monocrystalline metamaterials decreases (Fig. 4a). We determine the average linear crystal size present in a single metamaterial v_{crys} (Supplemental Material: *Crystal characterization*). This crystal size shows how large the side of an average crystal of a specific type is and is often used to indicate the size of crystals. Here, it represents a characteristic length-scale for the influence that a vertex has on its neighbors [33]. In Fig. 4c we show the distribution of the average crystal size in a metamaterial against κ for all the DS crystals with $\Theta = 0.25\pi$. Note that the thickness of the vertical lines in this graph shows the probability density of 100 simulations that we performed for each κ. We see that the average crystal size decreases when κ increases, even reaching zero for some cases at $\kappa > 10^{-0.4}$. This means that the stable

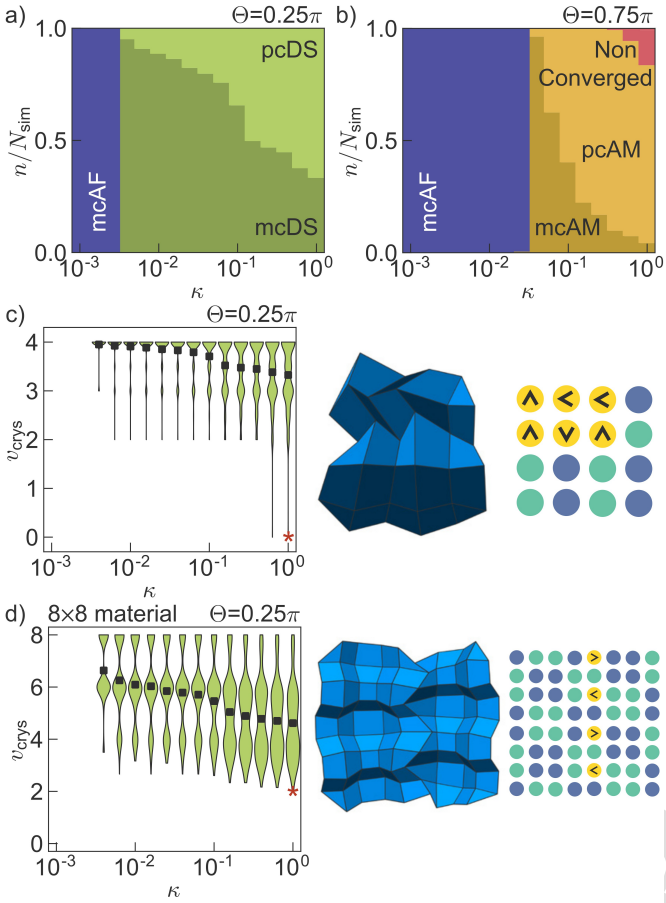

FIG. 4. a) Percentage of simulations (n/N_{sim}) for which the stable state is either monocrystaline or polycrystaline, indicated for each crystal type with a) $\Theta = 0.25\pi$ and with b) $\Theta = 0.75\pi$. Distribution of crystal size (v_{crys}) against κ for c) a 4×4 and d) a 8×8 material. The black dots represent the mean of the distribution. Examples (asterisk) of stable state with the lowest v_{crys}.

state of this metamaterial characterized by $v_{\text{crys}} = 0$ has no clearly defined crystal domains, and is only composed of defects (Fig. 4c). Following the analogy of 2D atomic crystal lattices, we find that the deformed state of the metamaterial is amorphous.

When repeating the same simulations for a larger metamaterial consisting of 8×8 vertices (Fig. 4d), we still observe this decrease in the crystal size with κ. However, we do not yet observe a metamaterial with $v_{\text{crys}} = 0$. The smallest crystal size we obtain is $v_{\text{crys}} = 2$, where the metamaterial consists only of unit cells that are separated by defects (Fig. 4d). Here it should be noted that the observed stable state in this example does not appear to be completely random, and is characterized by 2 regions of the same 4×4 periodicity, separated by a line of defects. We thus observe the importance of the material size, and more specifically, the effect that edges have on the stability and folding behavior of the crystal domains. On the one hand, for smaller sizes of the metamaterial, the edges dominate the behavior since they relax the face deformation of defects, and thus allow for more possible stable states. On the other hand, for a larger metamaterial the bulk behavior dominates and the face deformation is restricted by the neighbor vertices. Note that the same observations can be made for metamaterials with higher $\Theta = 0.75\pi$ (Supplemental Material: Fig. S10).

Importantly, these results indicate a change in behavior upon an increase of κ, from elastic origami with well defined crystals to an amorphous material with non-defined deformations. In contrast to the sudden transition from rigid origami to elastic origami observed for lower κ, the transition to an amorphous material appears to be continuous, and depends on the material size (Supplemental Material: Fig. S11).

Outlook.—In this work we show the rich behavior that appears in origami-inspired metamaterials when using bistable hinges. By applying methods that are often used to analyze defects in atomic crystal lattices, we are able to determine the most important parameters that affect the metamaterial's behavior, and identify three main regimes. *(i)* For weak bistability, hinge folding dominates face stretching and the metamaterial behaves according to a rigid description. *(ii)* Upon strengthening the bistability, a sudden transition occurs to periodic stable states that depend on face deformations, and that are the result of the elastic description. *(iii)* Strengthening the bistability further introduces defects, creating domain boundaries between several stable regions with decreasing crystal size, and leading to the point where the metamaterial's behavior becomes completely amorphous. These transitions are independent of metamaterial size, however edge effects can affect them at smaller sizes.

While we significantly simplified the allowed deformations in our models and only consider one lattice, we expect these transitions to occur in most origami-inspired metamaterials and even other foldable systems where elasticity, geometry and pres-stress (actuation) interact. Note that higher values of κ are not typically considered in engineering systems today, but we think that they can be achieved with new origami fabrication techniques using more responsive material such as liquid crystal elastomer [34], 3D printed hydrogel [35], inflatable soft robotic sheets [36], or by harnessing unstable behavior such as buckling [37]. Therefore, the identification of these three regions is important to determine how to control the folding behavior. While in case of rigid origami, a global stimulus could guide the folding behavior of the sheets, in case of elastic origami the stimulus needs to be distributed according to a length-scale governed by the characteristic crystal size. With these considerations one can place constraints on multistable metamaterial designs and their engineering realization at various length-scales.

This work is part of the Dutch Research Council (NWO) and was performed at the research institute

AMOLF. It is part of the research program Innovational Research Incentives Scheme Veni from NWO with project number 15868.

[1] S. Li, H. Fang, S. Sadeghi, P. Bhovad, and K. W. Wang, Advanced Materials **31**, 1805282 (2019).

[2] L. J. F. Sujan and D., World Academy of Science, Engineering and Technology **7**, 229 (2013).

[3] M. Johnson, Y. Chen, S. Hovet, S. Xu, B. Wood, H. Ren, J. Tokuda, and Z. T. H. Tse, Fabricating biomedical origami: a state-of-the-art review (2017).

[4] K. Kuribayashi, K. Tsuchiya, Z. You, D. Tomus, M. Umemoto, T. Ito, and M. Sasaki, Materials Science and Engineering A **419**, 131 (2006).

[5] Y. Liu, J. Park, R. J. Lang, A. Emami-Neyestanak, S. Pellegrino, M. S. Humayun, and Y. C. Tai, in *2013 Transducers and Eurosensors XXVII: The 17th International Conference on Solid-State Sensors, Actuators and Microsystems, TRANSDUCERS and EUROSENSORS 2013* (IEEE, 2013) pp. 1549–1552.

[6] J. T. Bruton, T. G. Nelson, T. K. Zimmerman, J. D. Fernelius, S. P. Magleby, and L. L. Howell, Royal Society Open Science **3** (2016).

[7] K. Miura, Title The Institute of Space and Astronautical Science Report **618**, 1 (1985).

[8] Z. Abel, J. Cantarella, E. D. Demaine, D. Eppstein, T. C. Hull, J. S. Ku, R. J. Lang, and T. Tachi, JoCG **7**, 171 (2015).

[9] T. C. Hull, in *Origami* (AK Peters, 2002) pp. 29–38, arXiv:1307.1065.

[10] C. D. Santangelo, Annual Review of Condensed Matter Physics **8**, 165 (2017).

[11] M. Stern, M. B. Pinson, and A. Murugan, Physical Review X **7**, 041070 (2017), arXiv:1703.04161.

[12] T. Tachi and T. C. Hull, Journal of Mechanisms and Robotics **9** (2017).

[13] P. Dieleman, N. Vasmel, S. Waitukaitis, and M. van Hecke, Nature Physics **16**, 63 (2020).

[14] J. T. Overvelde, J. C. Weaver, C. Hoberman, and K. Bertoldi, Nature **541**, 347 (2017).

[15] E. M. Arkin, M. A. Bender, E. D. Demaine, M. L. Demaine, J. S. Mitchell, S. Sethia, and S. S. Skiena, Computational Geometry: Theory and Applications **29**, 23 (2004).

[16] B. G. G. Chen and C. D. Santangelo, Physical Review X **8** (2018).

[17] A. Iniguez-Rabago, Y. Li, and J. T. Overvelde, Nature Communications **10**, 1 (2019).

[18] J. L. Silverberg, J. H. Na, A. A. Evans, B. Liu, T. C. Hull, C. D. Santangelo, R. J. Lang, R. C. Hayward, and I. Cohen, Nature Materials **14**, 389 (2015).

[19] B. Liu, J. L. Silverberg, A. A. Evans, C. D. Santangelo, R. J. Lang, T. C. Hull, and I. Cohen, Topological kinematics of origami metamaterials (2018).

[20] J. L. Silverberg, A. A. Evans, L. Mcleod, R. C. Hayward, T. Hull, C. D. Santangelo, and I. Cohen, Science **345**, 647 (2014).

[21] K. Liu, T. Tachi, and G. H. Paulino, Nature Communications **10**, 1 (2019).

[22] F. Lechenault and M. Adda-Bedia, Physical Review Letters **115**, 235501 (2015).

[23] E. T. Filipov and M. Redoutey, Extreme Mechanics Letters **25**, 16 (2018).

[24] S. Waitukaitis, R. Menaut, B. G. G. Chen, and M. Van Hecke, Physical Review Letters **114**, 055503 (2015).

[25] S. Waitukaitis and M. Van Hecke, Physical Review E **93**, 023003 (2016).

[26] M. B. Pinson, M. Stern, A. Carruthers Ferrero, T. A. Witten, E. Chen, and A. Murugan, Nature Communications **8**, 15477 (2017).

[27] C. Liu and S. M. Felton, Phys. Rev. Lett. **121**, 254101 (2018).

[28] J. A. Faber, A. F. Arrieta, and A. R. Studart, Science **359**, 1386 (2018).

[29] Y. Zhu and E. T. Filipov, Journal of Mechanisms and Robotics **12** (2020).

[30] S. Waitukaitis, P. Dieleman, and M. Van Hecke, Physical Review E **102** (2020).

[31] K. Bertoldi, V. Vitelli, J. Christensen, and M. Van Hecke, Nature Reviews Materials **2**, 1 (2017).

[32] A. Kelly and K. M. Knowles, *Crystallography and Crystal Defects: Second Edition* (John Wiley & Sons, Ltd, Chichester, UK, 2012).

[33] C. Coulais, C. Kettenis, and M. Van Hecke, Nature Physics **14**, 40 (2018).

[34] J.-H. Na, A. A. Evans, J. Bae, M. C. Chiappelli, C. D. Santangelo, R. J. Lang, T. C. Hull, and R. C. Hayward, Advanced Materials **27**, 79 (2015).

[35] Y. Xia, G. Cedillo-Servin, R. D. Kamien, and S. Yang, Advanced Materials **28**, 9637 (2016).

[36] J. Ou, M. Skouras, N. Vlavianos, F. Heibeck, C. Y. Cheng, J. Peters, and H. Ishii, UIST 2016 - Proceedings of the 29th Annual Symposium on User Interface Software and Technology , 121 (2016).

[37] K. Bertoldi, P. M. Reis, S. Willshaw, and T. Mullin, Advanced Materials **22**, 361 (2010).

Declaration of interests

☒ The authors declare that they have no known competing financial interests or personal relationships that could have appeared to influence the work reported in this paper.

☐ The authors declare the following financial interests/personal relationships which may be considered as potential competing interests: